NANO · MICRO small
www.small-journal.com

Autonomous Magnetic Microrobots by Navigating Gates for Multiple Biomolecules Delivery

Xinghao Hu, Byeonghwa Lim, Sri Ramulu Torati, Junjia Ding, Valentine Novosad, Mi-Young Im, Venu Reddy, Kunwoo Kim, Eunjoo Jung, Asif Iqbal Shawl, Eunjoo Kim, and CheolGi Kim**

The precise delivery of biofunctionalized matters is of great interest from the fundamental and applied viewpoints. In spite of significant progress achieved during the last decade, a parallel and automated isolation and manipulation of rare analyte, and their simultaneous on-chip separation and trapping, still remain challenging. Here, a universal micromagnet junction for self-navigating gates of microrobotic particles to deliver the biomolecules to specific sites using a remote magnetic field is described. In the proposed concept, the nonmagnetic gap between the lithographically defined donor and acceptor micromagnets creates a crucial energy barrier to restrict particle gating. It is shown that by carefully designing the geometry of the junctions, it becomes possible to deliver multiple protein-functionalized carriers in high resolution, as well as MCF-7 and THP-1 cells from the mixture, with high fidelity and trap them in individual apartments. Integration of such junctions with magnetophoretic circuitry elements could lead to novel platforms without retrieving for the synchronous digital manipulation of particles/biomolecules in microfluidic multiplex arrays for next-generation biochips.

1. Introduction

The precise manipulation of single fluid droplets, individual particles, cells, and biomolecules has attracted fundamental and clinical interest because of the vast applications in biochemical detection, gene sequencing, and single-cell analysis.[1–5] Here, a synchronous sorting and trapping platform is an essential feature for in situ digital manipulation of these biomolecules. Even though the microfluidic chip technology[6–8] has presented outstanding performances to sort a large number of analyte, the disabilities in flexible manipulation and parallel-automated isolation restrict on-chip applications for conducting further analyses to rare analyte. So far, various other manipulation approaches employing optical,[9–13] electrical,[14,15] magnetic,[16–22] acoustic,[23,24] mechanical,[25,26] and moisture-responsive[27–29] forces have also been developed in lab-on-a-chip platforms.

Among the controllable approaches for the digital manipulation of arrays of rare analyte from polydisperse mixtures, magnetic manipulation technology implemented by well-designed micromagnets has significant advantages in the massively parallel and logical control,[19,20] because the operation logic is similar to the well-known bubble domain control method in the recording memory.[30] Furthermore, developed magnetic manipulation techniques have tended to focus on the separation of magnetic particles through the designed patterns, where the particles play a role as microrobots to transport biomolecules. However, semiautomatic separation,[16,19,31,32] low efficiency of separation,[19,33] and incompetent individual trapping[33–37] restrict the implementation of synchronous high-resolution separation and localization of parallel biofunctionalized objects in the practical on-chip applications.

Herein, inspired by the concept of quantum electron tunneling in a conductor/insulator/conductor junction, a classical junction (JCT) composed of magnetic-donor/nonmagnetic/magnetic-acceptor (M/NM/M) elements has been proposed and demonstrated for synchronous self-navigating and delivery of biofunctionalized microrobotic particles (PRT) in magnetophoretic platform (**Figure 1**a), under a rotating in-plane magnetic field (Figure S1a, Supporting Information), H_{app}. The navigating tracks are defined depending on the intrinsic properties (size and magnetic susceptibility) of the particle microrobots. The sorting efficiency of navigation JCTs is dependent on the geometries of the donor (P_d) and acceptor (P_a) micromagnets

Dr. X. Hu, Dr. B. Lim, Dr. S. R. Torati, Dr. M.-Y. Im, Dr. V. Reddy, Dr. K. Kim, E. Jung, Dr. A. I. Shawl, Prof. C. Kim
Department of Emerging Materials Science
DGIST
Daegu 42988, Republic of Korea
E-mail: cgkim@dgist.ac.kr
Dr. J. Ding, Dr. V. Novosad
Materials Science Division
Argonne National Laboratory
Argonne, IL 60439, USA
E-mail: novosad@anl.gov
Dr. M.-Y. Im
Center for X-ray Optics
Lawrence Berkeley National Laboratory
Berkeley, CA 94720, USA
Dr. E. Kim
Nano-Bio-materials Division
DGIST
Daegu 42988, Republic of Korea
The ORCID identification number(s) for the author(s) of this article can be found under https://doi.org/10.1002/smll.201800504.

DOI: 10.1002/smll.201800504

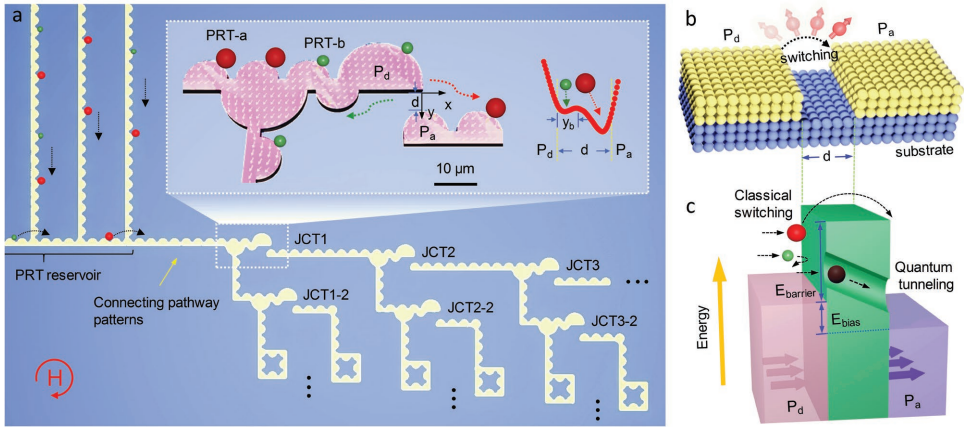

Figure 1. Principle and performance of M/NM/M junctions for autonomous navigating tracks of robotic particles. a) Perspective view of collection pad and magnetic/nonmagnetic/magnetic junctions (JCTs) for autonomous delivery to individual apartments. Inset presents the sorting schematic of JCT. b,c) Conceptual diagram for particle switching, and energy conditions at JCT with positive potential barrier ($E_{barrier}$) and bias (E_{bias}) for donor (P_d) and acceptor (P_a) patterns.

(Figure S1b, Supporting Information), the size of nonmagnetic gap (d), and the rotating frequency or strength of the magnetic field. As proof of concept, we have tested the performance of the developed serial JCTs for autonomous delivery of robotic protein-functionalized particles to individual apartments (APT), and here even nominal same particles can be separated efficiently. In addition, we have demonstrated a separation of MCF-7 (human breast cancer cells) and THP-1 (human monocytic cells) cells conjugated with different carrier particles from the polydisperse mixture using the devised JCTs.

2. Results and Discussion

2.1. Dimensional and Topological Gating for Autonomous Delivery Tracks

The microrobotic particles can be trapped by field gradients at the periphery of reservoir patterns and transported to JCTs along successive minimum energy locations under H_{app} in clockwise direction (Figure S1c, Supporting Information). At JCTs, the nonmagnetic gap causes the energy barrier to hinder the particle transportation (Figure 1a, inset), but the particles with higher transporting energy can cross over the barrier, resulting in the particle conducting junction (Figure 1b,c). The nonlinear dynamics of particles moving around the periphery of a micromagnet have revealed two different dynamical modes: phase-locked mode at low driving frequencies and phase-slipping mode above the critical frequency.[38] Thus, the particles as autonomous microrobots have self-selection to transportation tracks. Two types of switching mechanisms have been achieved as particle gating in the present work: dimensional gating (Figure S2a–c, Supporting Information), and topological gating regardless of dimensions (Figure S2d–f, Supporting Information). The dimensional gating allows sorting the particles based on their size, where the rotating field frequency lower than the critical frequency (f_c) regulates the constant phase lag between the particle position and the H_{app} direction,[39] termed as "phase-locked mode." In this mode, particles transport in contact with the pattern edge. Thus, particles with a radius r smaller than the barrier distance (y_b) cannot cross over the barrier to the P_a from P_d at JCT. However, the particles with a radius r larger than y_b can cross over the barrier and switch to P_a, and then continuously move along the P_a track (Movie S1, Supporting Information).

Topological gating works at a frequency higher than f_c. When the frequency of the rotating magnetic field is increased, the phase lag also increases. Then when reaching to f_c, the modulation from the "phase-locked" to "phase-slipping" modes occurs. The accompanied particle jumping during the phase modulation allows the topological gating even for the particles of radii smaller than y_b. Hence, using an intermediate operating frequency between two critical frequencies, f_{c1} for low-χ particles and f_{c2} for high-χ particles, two types of particles can be separated because the particles with high-χ are in the phase-locked mode, and move along the P_d track, while the low-χ particles are in the phase-slipping mode and thus hop to the P_a track. Furthermore, the nominal same particles due to heterogeneity can also be separated (Movie S2, Supporting Information).

2.2. Donor and Acceptor Patterns Optimization for Universal Switching Junctions

The performance of the sorting JCTs is strongly correlated with several main parameters: geometry and combination of P_d and P_a, particle properties regarding the size and the magnetic susceptibility, and the gap size at JCTs. **Figure 2**a presents the change of potential energy at tailored (Q_t) and circular (Q_c) peripheries with shape variation (t) from the half-disk micromagnet which corresponds to $t = 0$. The energy density at both Q_t and Q_c decreases with decreasing t, but their difference determining the bias energy increases. Specifically, four lunar shapes of isolated micromagnets: full-, three-quarter-, half-, and crescent-shaped disk patterns, have been fabricated to investigate the geometry effect. Initially, the domain structures of the patterned four micromagnets were observed and simulated for

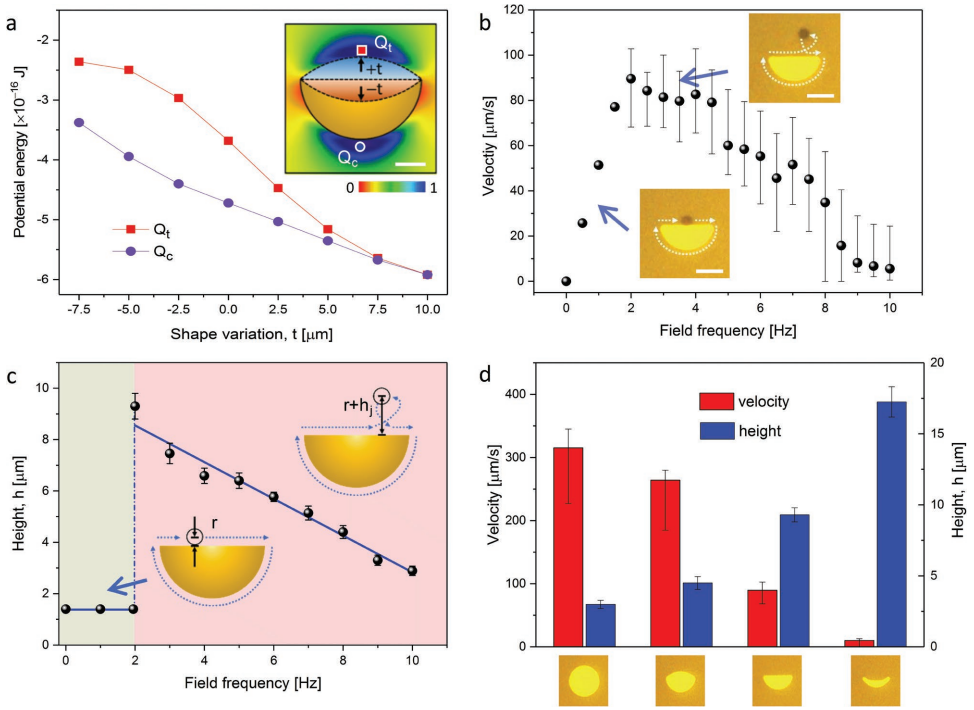

Figure 2. Robotic particle dynamics around lunar-shaped micromagnets. a) Potential energy at two poles (Q_t and Q_c) versus shape variation (t) from the half-disk micromagnet which corresponds to $t = 0$. Inset depicts the energy distribution around the micromagnet (the scale bar is 5 μm). The multiplication factor for color bar is 6.0×10^{-16} J. b) Particle velocity (the scale bars of insets are 10 μm) and c) jumping height as a function of the rotating field frequency under an 8.5 mT field for lunular (half-disk-shaped) micromagnets 20 μm in diameter. The insets show images of particle motion in the phase-locked and phase-slipping modes, where the jumping location and height of the particles are determined by tracking the motion trajectory. d) Maximum velocity and normal height of the particles with respect to the micromagnet peripheries for the four lunar micromagnet shapes. For the crescent-shaped disk micromagnet, the normal height of the particle is divided into two components: the height in the phase-locked mode below the yellow horizontal line and the jumping height in the phase-slipping mode.

understanding the variations in the magnetic configuration (Figures S3 and S4, Supporting Information). The potential barrier and bias energy for several combinations of two micromagnets based on the energy distribution of the individual patterns were investigated (Figures S5–S7, Supporting Information). From these results, we found that only the combination of the flat and curved edges of half-shaped patterns is suitable for P_d and P_a patterns consisting in the universal switching junction because of the positive values of $E_{barrier}$ and E_{bias} (Table S1, Supporting Information).

Considering the particle nonlinear dynamics, the particle velocity increases linearly with increasing rotating frequency when the frequency is less than the particle f_c, as shown in Figure 2b. However, the particle velocity decreases with increasing the frequency above f_c because the particles enter into the phase-slipping mode, starting to jump at the flat edge of the half-disk micromagnet (Figure 2b, inset), corresponding to the maximum velocity of the particles (≈90 μm s^{-1}) under an 8.5 mT field. The error bars of the particle velocity indicate the absolute deviations from 20 particles measured for a good statistics. The maximum velocity to a full-disk micromagnet (≈315 μm s^{-1}) is larger than that of a half-disk, but the jumping location is random (Figure S8a and Movie S3, Supporting Information). Moreover, the jumping height (h) of the particles is also significant to the particle hopping at the JCT. The jumping height at f_c for a half-disk is ≈10 μm, which decreases with increasing the rotating frequency shown in Figure 2c (Movie S4, Supporting Information), but it is larger than that of the full-disk (≈3 μm) shown in Figure 2d. As a result, by considering the dynamic characteristics of particles, including particle velocity (Figure S8, Supporting Information), jumping height (Figure 2d), and the controllable jumping location (Figure S8 and Movie S3, Supporting Information), the lunular geometry of the micromagnet (half-disk) shows the best situation for particle jumping around the four lunar shapes of isolated micromagnets.

2.3. Particles Dynamics to Isolated Lunular Micromagnets

To choose a suitable frequency for particle sorting, we investigated the dynamic characteristics around the isolated lunular micromagnets for three types of particles with radii of 1.4, 2.25, and 2.9 μm, corresponding to the magnetic susceptibility of 0.50, 0.62, and 0.06 (SI), respectively (Figure S9a, Supporting Information). **Figure 3**a presents the calculated phase diagram of the critical frequencies (proportional to field strength, Figure S9b (Supporting Information) based on particle size and magnetic susceptibility under an 8.5 mT field (see model of the critical frequency, Supporting Information). For the f_c curve at the 1 Hz rotating field, the particles corresponding to the parameters above the white line are in the phase-locked

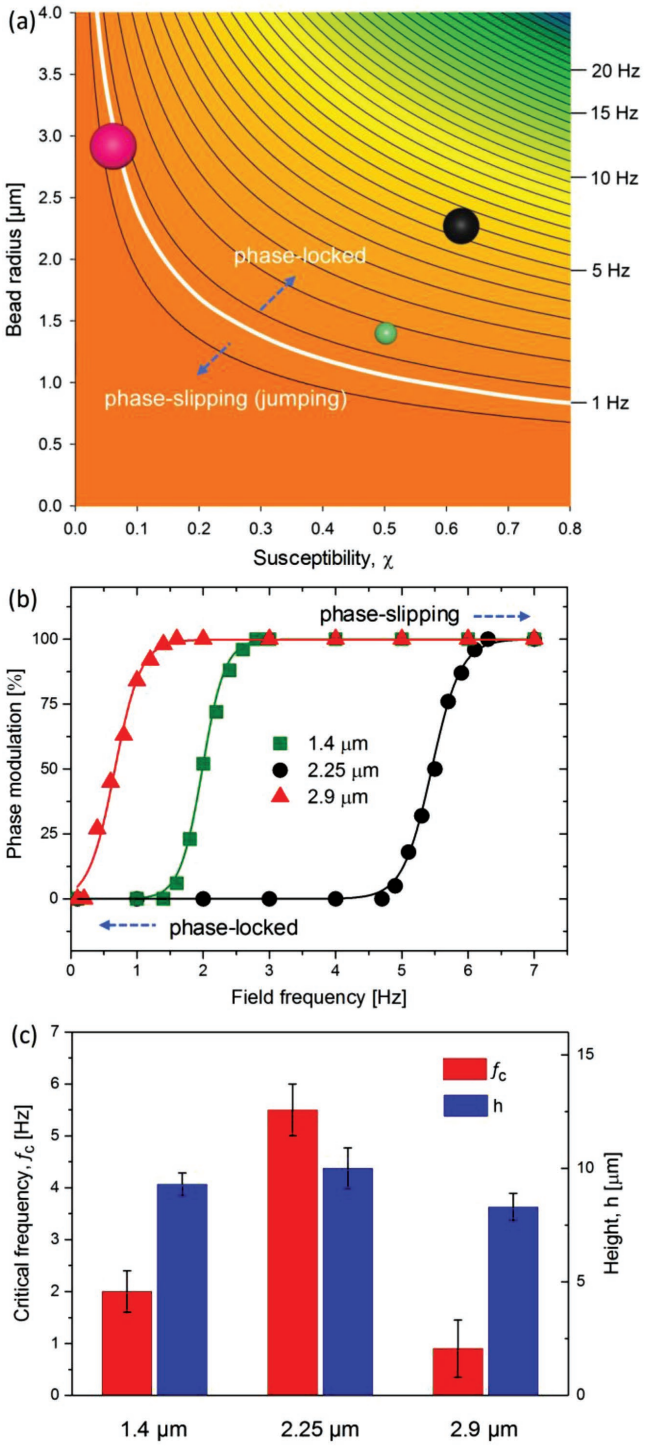

Figure 3. Critical frequencies of robotic particle phase modulation for an isolated lunular micromagnet. a) Phase diagram of the critical frequencies for isolated lunular micromagnet based on the parameters of particle size and magnetic susceptibility under an 8.5 mT field. Three types of particles with radii of 1.4, 2.25, and 2.9 μm are indicated as green squares, black circles, and red triangles, respectively. b) Topological mode modulation from the phase-locked to phase-slipping mode for the three types of particles under an 8.5 mT field as a function of field frequency. c) Corresponding critical frequencies (f_c) and normal heights (h) of the three types of particles.

mode, while particles with parameters below the white line are in the phase-slipping mode.

The modulation ratio from phase-locked to phase-slipping for three types of particles as a function of the driving field frequency is shown in Figure 3b. In the experiment, 50 particles of each size were examined. Due to the heterogeneity in particle size and magnetic susceptibility, a deviation of the critical frequency was observed. For the 2.9 μm radius particles, the modulation ratio of the phase-slipping mode is increased from 0.2 Hz, reaching 100% at 1.6 Hz. Similarly, the critical frequencies of the 1.4 and 2.25 μm radius particles are in the ranges of 1.4–2.8 and 4.7–6.3 Hz, respectively.

The mean critical frequencies of particles with radii of 1.4, 2.25, and 2.9 μm are 2.0, 5.5, and 0.9 Hz, respectively, under an 8.5 mT field, and their normal jumping heights at the critical frequencies are plotted in Figure 3c. The critical frequency is proportional to the applied field strength shown in Figure S8b (Supporting Information). Furthermore, the jumping heights of the particles with radii of 1.4, 2.25, and 2.9 μm were measured as 9.3, 10.0, and 8.3 μm, respectively, indicating that the jumping height does not depend on particle size but rather is related to their magnetic susceptibility.

2.4. Switching Characteristics of Lunular Junctions

The gap size between P_d and P_a is crucial to the particle sorting. **Figure 4**a shows the energy barrier position as a function of the gap size, which indicates that the JCTs to the particle path can be divided into three scenarios: conducting, semiconducting, and insulating JCTs, similar to electron tunneling transportation in conductor/insulator/conductor junctions. When the gap size is smaller than 3 μm, there is a single energy well at the periphery of P_d, and thus all particles regardless of their dimension or magnetic susceptibility, can switch to P_a from P_d (conducting junction). The energy barrier appears when the gap size is larger than 3 μm and the barrier distance increases with increasing gap size (semiconducting junction). Analogous to electron tunneling through a barrier with the aid of thermal, light, or electrical excitation, the switching ability can be adjusted by particle size, rotating frequency of the field, or the field strength. As shown in Figure 4b for the JCT with a 5 μm gap, the simulated energy evolution as a function of the rotating field angle reveals the two separated energy minima around 30° field from the y-axis (Figure 4b, iv and v). Here, a particle with a 1.4 μm radius follows the local energy minima along the P_d track (Figure 4c), but a particle with a radius of 2.5 μm can cross the energy barrier and follows the local energy minima along the P_a track (Figure 4d). On the other hand, a particle in the phase-slipping mode can hop to the P_a track, even though the radius is smaller than the barrier distance. However, when the barrier distance is larger than the jumping height, the particle cannot hop to the P_a track (insulating junction).

Patterned micromagnet JCTs with various gap sizes have been fabricated to evaluate the particle switching efficiency from P_d to P_a. Here, 50 particles with each radii of 1.4, 2.25, and 2.9 μm were tested to ensure a good statistics. Figure 4e shows the switching ratio as a function of the gap size under a 0.2 Hz field, at which frequency all particles are in the

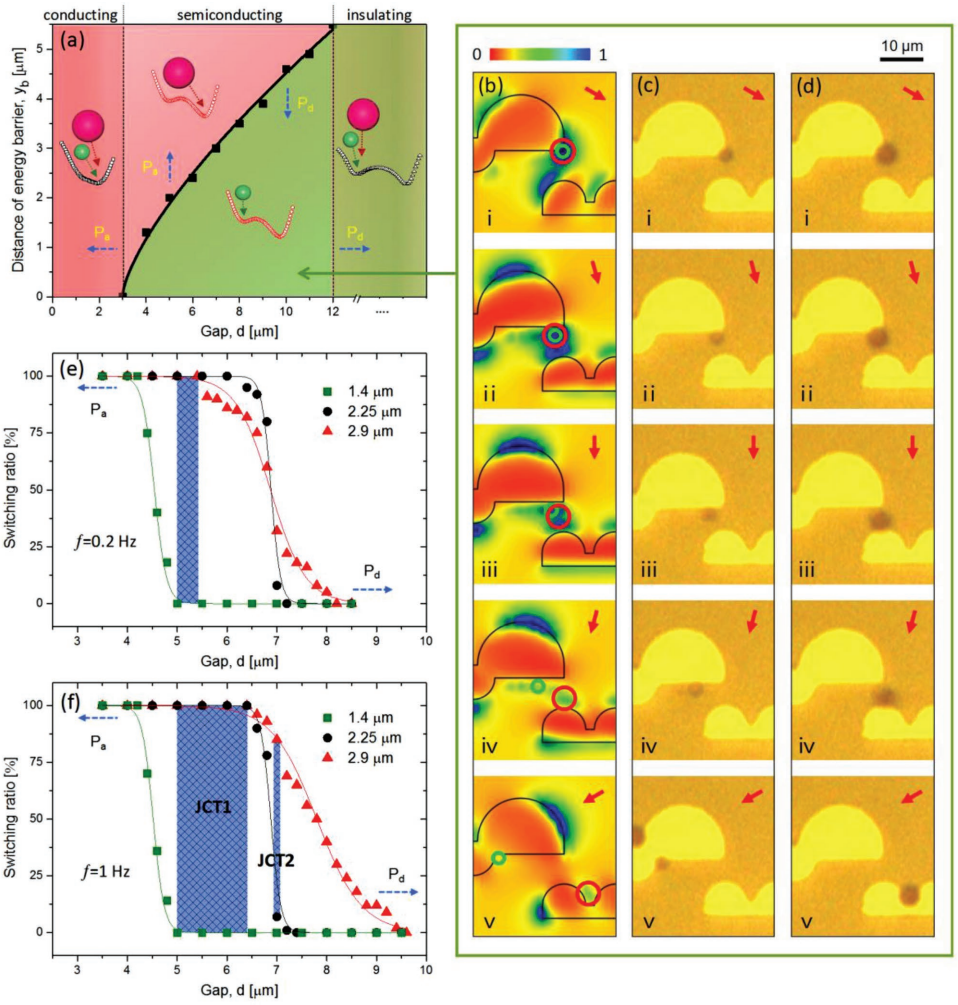

Figure 4. Switching characteristics of particles at the M/NM/M junction. a) The dependence of the barrier distance (y_b) on the gap size between the donor P_d and acceptor P_a patterns. JCT with less than 3 μm gap exhibits no energy barrier, and all particles at P_d move to the acceptor P_a (conducting junction). Gap size larger than 3 μm, resulting in an energy barrier centered at y_b, enables the gating of particles via different sizes and magnetic susceptibilities (semiconducting junction). However, for gaps larger than the threshold, none of the particles can switch to pattern P_a, even in jumping mode (insulating junction). b) Simulated energy evolution for a 5 μm gap, where two energy minima are revealed at the periphery of the donor and acceptor patterns, resulting in a semiconductor junction. c) Trace of a small particle navigating along the donor pattern. d) Trace of a navigating particle that cross the barrier to the acceptor pathway. The multiplication factor for color bar is 6.5×10^{-16} J. e,f) Measured switching ratios of three types of particles depending on the gap size under an 8.5 mT field at 0.2 and 1 Hz, respectively.

phase-locked mode (Figure 3a,b). The switching ratio of the 1.4 μm radius particles to the P_a track is 100% for a 4.2 μm gap (corresponding to a barrier distance of 1.3 μm), and the ratio decreases with increased gap size. The switching ratio finally reaches 0% at a 5.0 μm gap, corresponding to a 2.0 μm barrier distance. Similarly, switching characteristics for the 2.25 and 2.9 μm particles are observed for gap sizes in the range of 6.0–7.1 and of 5.4–8.2 μm, respectively. Hence, the 1.4 μm particles can be separated 100% from 2.25 and 2.9 μm particles for the range of gap sizes (5.0–5.4 μm) marked in blue (Figure 4e).

There is overlapping of the switching efficiency for the 2.25 and 2.9 μm radii particles around the 7 μm gap (Figure 4e), where a wide dispersion in the gap size is revealed to the 2.9 μm radius particles. Such a switching overlap between these two sizes of particles is unexpected considering the principle of dimensional gating. However, the measured size distribution of the 2.9 μm particles is relatively wide compared with that of the 2.25 μm radius particles (Figure S10, Supporting Information). Thus, an efficient separation by dimensional gating is not achieved for particles with mean radii of 2.25 and 2.9 μm.

On the other hand, the 2.25 and 2.9 μm radii particles have different susceptibilities resulting in different f_c (Figure 3a). Hence, using topological gating, the two types of particles can be separated effectively when the 2.25 μm particles are in the phase-locked mode, moving along the P_d track at a 1 Hz frequency, but the 2.9 μm particles are in the phase-slipping mode, hopping to the P_a track. For a 7.0 μm gap size with a 3.5 μm barrier distance, the switching ratios were measured as 7 and 85% for the 2.25 and 2.9 μm particles, respectively (Figure 4f). As a result, each of three nominal same particles can also be separated efficiently with increasing the gap size as shown in Figure S10c (Supporting Information).

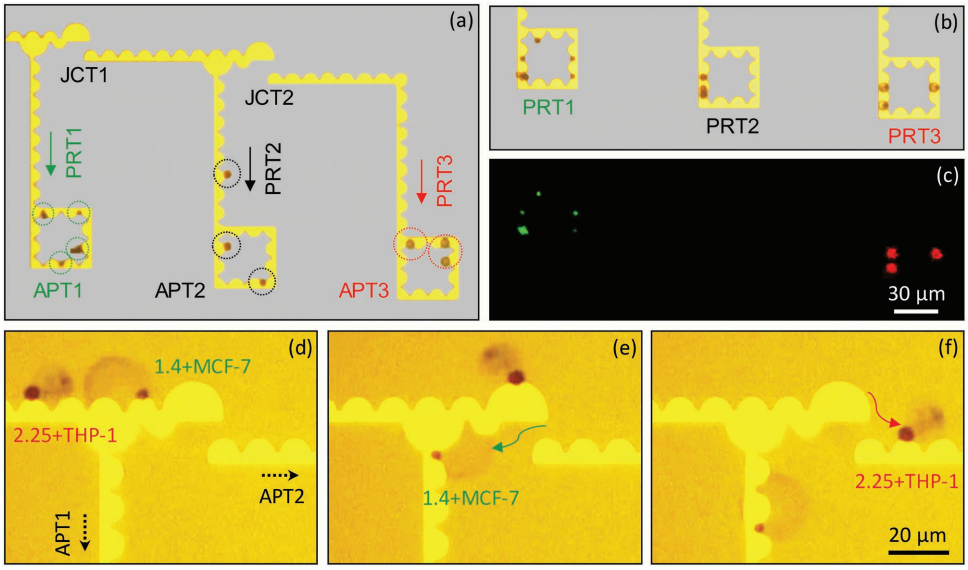

Figure 5. Autonomous delivery of robotic particles to individual apartments. a) Three types of robotic particles with 1.4, 2.25, and 2.9 μm radius, are delivered to the desired individual apartments by a dimensional gating through JCT1 (5.2 μm gap) and a topological gating through JCT2 (7 μm gap) under an 8.5 mT field at 1 Hz frequency. b,c) Bright-field and fluorescent images of the trapped particles in the individual apartments. Here, the 1.4 (green), 2.25 (black), and 2.9 μm (red) radius particles were coated with anti-GFP, anti-B220, and anti-RFP, respectively. d–f) Snapshot for separating MCF-7 and THP-1 cells conjugated with 1.4 and 2.25 μm radius particles, respectively, using a dimensional gating JCT2 with a 5.2 μm gap at 0.2 Hz.

2.5. Synchronous Sorting and Trapping of Multiple Biofunctionalized Particles

It is possible to sort target particles from a mixture by combining multiple dimensional- and topological-gating JCTs. For example, the sorting device consists of two proposed JCTs, using a dimensional gating JCT1 with a gap size in the range of 5–6.5 μm, and a topological gating JCT2 with a 7 μm gap. A mixture containing three types of biofunctionalized particles (1.4, 2.25, and 2.9 μm radii) has been separated and transferred to three individual apartments consisting of closed half-disk patterns (Movie S5, Supporting Information). Under a 1 Hz rotating field of 8.5 mT, the particles with 1.4 and 2.25 μm radii are in the phase-locked mode, while the 2.9 μm radius particles are in the phase-slipping mode. Thus, the 1.4 μm particles cannot cross over the dimensional gate of JCT1 guided to APT1. However, both the 2.25 and 2.9 μm particles can cross over JCT1, and navigate along the *x*-direction.

The 2.25 μm radius particles in the phase-locked mode follow along the track to APT2, while the 2.9 μm radius particles in the phase-slipping mode hop JCT2 by topological gating and then navigate to APT3 shown in **Figure 5**a (Movie S6, Supporting Information). Bright-field and fluorescent images of the three types of trapped particles in the individual apartments are presented in Figure 5b,c. Here, the 1.4 (green), 2.25 (black), and 2.9 μm (red) radius particles were coated with anti-GFP, anti-B220, and anti-RFP, respectively. Furthermore, as a proof for cell separation, the sorting of two types of cells such as MCF-7 and THP-1 cells conjugated with 1.4 and 2.25 μm radius particles, respectively, has also been demonstrated using dimensional gating under the 0.2 Hz frequency field in Figure 5d–f (Movie S7, Supporting Information). Further analysis about the separation of conjugated cells is presented in Figure S11 (Supporting Information).

3. Conclusion

Inspired by the electron tunneling junction of conductor/insulator/conductor, we developed a micromagnet junction consisted of donor and acceptor patterns with a nonmagnetic gap, for autonomous delivery of multiple biofunctionalized microrobotic particles to individual apartments. The combination of the lunular flat and circular-edged micromagnets affords an universal junction criteria both for dimensional and topological gating separation with high resolution. Even nominal same particles can be sorted and localized at microscale regions on chip, which should be exceedingly significant to tiny force evaluation in biophysical studies such as torsional stiffness in DNA,[40,41] surface adhesion,[42] friction force at nano-bio interfaces,[39] as well as polymerase chain reaction (PCR) on a chip.[43] The main advantage of the proposed system is the successive delivery of biofunctionalized robotic particles via dimensional and topological gating with high fidelity, and their synchronous trapping in separated apartments for individual analysis without retrieving. Further integration of the serial micromagnet junctions with magnetophoretic circuits could lead to a novel platform for in situ autonomous delivery of biomolecules by the particle microrobots in multiplex arrays required in next-generation biochips.[1]

4. Experimental Section

Fabrication of Micromagnets and Rotational Field Setup: Silicon wafers were cleaned by acetone and methanol 1 h for each, and then were dried by nitrogen blow. Photoresist (AZ 5214 E) was spun onto the wafers for 5 s at 1000 rpm, followed by 30 s at 3000 rpm using a spin coater (MIDAS, SPIN-12000). A prebake was performed at 120 °C for 55 s on a hotplate (AS ONE, TH-900). The wafers were then exposed to ultraviolet

light for 7 s by a mask aligner (MIDAS, MDA-400S). The patterns were developed in AZ 500 MIF at room temperature for 1 min. Chips were then rinsed with deionized water and dried with nitrogen.

The film deposition was performed using conventional DC sputtering system. The base pressure of the sputtering system was 3×10^{-7} Torr and the sputtering process was carried out at 3×10^{-3} Torr. The seed layer was a 5 nm thick Ta film. Next, 100 nm thick $Ni_{83}Fe_{17}$ (Kojundo Chemical Laboratory Co., Ltd., Japan) was deposited. Subsequently, the chips were immersed 30 min in acetone. Then the chips were exposed to 10 s of sonication in an ultrasonic bath, rinsed using acetone, and dried with nitrogen. The chips were then coated with 0.5 µm thick Teflon (DuPont, Grade 601S2-100-6) by spin-coating at 3500 rpm for 30 s to protect the pattern from contamination due to the outside environment and to diminish surface adhesion forces.

A rotating magnetic field was generated by ferrite core solenoids, which were arranged at mutually orthogonal axes (*x*–*y*) with respect to the substrate. Two current sources were controlled by LabVIEW (National Instruments) to supply sinusoidal waveforms to each solenoid coil in the orthogonal axes, whose phase difference was adjusted by 90° to generate a rotating magnetic field in the *x*–*y* plane.

Magnetic Domain Observation and Simulation: For a fundamental understanding of the magnetic states for the four geometries and the lunular junction, the magnetic domains were observed under a cyclic field strength by full-field magnetic transmission soft X-ray microscopy (MTXM), including a comparison with simulation using mumax[3] software. For domain observations, three-quarter-, half-, and crescent-shaped disk micromagnets were designed by cutting the upper side of a full-disk micromagnet with a diameter of 5 µm due to the beam size limitation of the MTXM. The domain observation was performed under the cyclic field in a fixed direction.

Biofunctionalized Magnetic Particles: Superparamagnetic particles of 1.4 µm (Dynabeads M-280) and 2.25 µm radii (Dynabeads Mouse Pan B) were purchased from Invitrogen, and 2.9 µm radius particles (CM01N/11374) were procured from Bangs Laboratories. The 1.4 and 2.9 µm radius particles were labeled with green and red fluorescent protein, respectively, for surface biomolecular identification. To label the proteins, 0.01 mL streptavidin-functionalized magnetic particles with diameters of 2.8 µm (10 mg mL^{-1}) and 5.8 µm (10 mg mL^{-1}) were washed thrice with PBS buffer (pH 7.4). After thorough washings, the particles were resuspended in PBS buffer (0.99 mL, pH 7.4) with 0.01 mL (100 µg mL^{-1}) of biotin-labeled antibodies of green fluorescent protein (anti-GFP, abcam-ab6658) and red fluorescent protein (anti-RFP, abcam-ab34771), respectively, and then incubated under rotation for 30 min at room temperature. The resulting (anti-GFP/anti-RFP) antibody-conjugated (Dynabeads M-280/Bangs particles) particles were isolated from the excess antibody solution using an external magnetic field and resuspended in 1 mL of PBS buffer (pH 7.4).

Binding of HLA-A2/EpCaM Antibodies to the Magnetic Particles: HLA-A2 and EpCaM antibodies were bound to the 2.25 (tosyl-activated) and 1.4 µm (carboxyl-coated) radius particles, respectively. Here, 20 µL volumes of both particles were washed with PBS (pH 7.4) three times. After washing, the particles were resuspended in 1 mL of PBS with 0.02% Tween-20. Final concentrations of 4×10^{-6} M EDC (30 µL) and 10×10^{-6} M sulfo-NHS (30 µL) were added to the washed Dynabeads in PBS. The above solution was mixed well and kept in a rotator for 15–20 min. Then, the resultant EDC-NHS-activated particles were collected using a magnet and were washed three times with PBS (+0.02% Tween-20). Human leukocyte antigen serotype A2 (HLA-A2)/epithelial cell adhesion molecule (EpCAM) antibody was added to the activated particles, and the particles were kept in a rotator for 2–3 h at room temperature. The particles were washed three times with PBS using a magnet to remove unbound antibody. The resultant antibody-bound particles were resuspended in 1 mL of PBS buffer and stored at 4 °C.

Cell Culture and Growth: THP-1 (ATCC TIB-202D) cells of a human monocytic cell line were grown in RPMI 1640 medium supplemented with 10% fetal bovine serum (FBS), 1% penicillin/streptomycin and 2-mercaptoethanol to a final concentration of 0.05×10^{-3} M. Cell cultures were established by 2–4 $\times$ 10^5 viable cells mL^{-1}. The cultures were maintained in 100 mm dishes with the addition of fresh medium or the replacement of medium every 2–3 d. The cells were subcultured when the concentration reached 8×10^5 cells mL^{-1}.

MCF-7 (ATCC HTB-22) cells, from a human breast adenocarcinoma cell line, were reported to express EpCAM biomarker on the surface. They were grown in DMEM supplemented with 10% FBS and 1% penicillin/streptomycin. The medium was changed by gently removing the medium and adding fresh medium every 2–3 d. Cell subculturing was performed by carefully removing the medium, and 0.25% (w/v) trypsin and 0.53×10^{-3} M EDTA solution were added to the cell layer for ≈5–7 min at 37 °C. After incubation for 5–7 min, 5–8 mL medium was added, and the cells were gently pipetted. The cells were centrifuged at 1000 rpm for 5 min, and the supernatant was discarded. Then, the cells were resuspended in fresh DMEM and subcultivated at 1:3 to 1:6 ratios. Cells were authenticated using short tandem repeat profiling and tested for mycoplasma.

Cells and Superparamagnetic Particles Binding: THP-1 cells at a concentration of 1×10^{-4} cells mL^{-1} and MCF-7 cells at a concentration of 1×10^{-5} cells mL^{-1} were centrifuged, the medium was replaced with PBS (+0.02% Tween-20), and the cells were then washed twice with PBS. The cells were added to 100 µL of antibody-bound particles and kept in a rotator for 30 min at room temperature. After incubation, the cells with the antibody-coated particles were washed thrice with PBS using an external magnet to separate the cells that were not bound to the magnetic particles, and the particles bound to cells were then resuspended in fresh PBS for further experiments. The binding of the magnetic particles to the cells was confirmed using an optical microscope.

Supporting Information

Supporting Information is available from the Wiley Online Library or from the author.

Acknowledgements

This work was supported by the Samsung Research Funding Center of Samsung Electronics under Project No. SRFC-MA1402-01, and DGIST R&D program of the Ministry of Science, ICT and Future Planning (17-BT-02). Work at Argonne was supported by the U.S. Department of Energy (DOE), Office of Science, Basic Energy Sciences (BES) under Award # DE-AC02-06CH11357. Work at the ALS was supported by the Director, Office of Science, Office of Basic Energy Sciences, Scientific User Facilities Division of the U.S. Department of Energy under Contract No. DE-AC02-05CH11231.

Conflict of Interest

The authors declare no conflict of interest.

Keywords

biofunctionalization, cells sorting, lab-on-a-chip, microparticles manipulation, microrobots

Received: February 5, 2018
Revised: March 17, 2018
Published online: May 8, 2018

[1] J. El-Ali, P. Sorger, K. Jensen, *Nature* **2006**, *442*, 403.
[2] F. Vollmer, S. Arnold, *Nat. Methods* **2008**, *5*, 591.

[3] J. Eid, A. Fehr, J. Gray, K. Luong, J. Lyle, G. Otto, P. Peluso, D. Rank, P. Baybayan, B. Bettman, A. Bibillo, K. Bjornson, B. Chaudhuri, F. Christians, R. Cicero, S. Clark, R. Dalal, A. deWinter, J. Dixon, M. Foquet, A. Gaertner, P. Hardenbol, C. Heiner, K. Hester, D. Holden, G. Kearns, X. Kong, R. Kuse, Y. Lacroix, S. Lin, P. Lundquist, C. Ma, P. Marks, M. Maxham, D. Murphy, I. Park, T. Pham, M. Phillips, J. Roy, R. Sebra, G. Shen, J. Sorenson, A. Tomaney, K. Travers, M. Trulson, J. Vieceli, J. Wegener, D. Wu, A. Yang, D. Zaccarin, P. Zhao, F. Zhong, J. Korlach, S. Turner, *Science* **2009**, *323*, 133.
[4] N. Navin, J. Kendall, J. Troge, P. Andrews, L. Rodgers, J. McIndoo, K. Cook, A. Stepansky, D. Levy, D. Esposito, L. Muthuswamy, A. Krasnitz, W. R. McCombie, J. Hicks, M. Wigler, *Nature* **2011**, *472*, 90.
[5] C. Ma, R. Fan, H. Ahmad, Q. Shi, B. Comin-Anduix, T. Chodon, R. C. Koya, C.-C. Liu, G. A. Kwong, C. G. Radu, A. Ribas, J. R. Heath, *Nat. Med.* **2011**, *17*, 738.
[6] N. Pamme, A. Manz, *Anal. Chem.* **2004**, *76*, 7250.
[7] J. D. Adams, U. Kim, H. T. Soh, *Proc. Natl. Acad. Sci. USA* **2008**, *105*, 18165.
[8] N. M. Karabacak, P. S. Spuhler, F. Fachin, E. J. Lim, V. Pai, E. Ozkumur, J. M. Martel, N. Kojic, K. Smith, P. Chen, J. Yang, H. Hwang, B. Morgan, J. Trautwein, T. A. Barber, S. L. Stott, S. Maheswaran, R. Kapur, D. A. Haber, M. Toner, *Nat. Protoc.* **2014**, *9*, 694.
[9] A. Ashkin, J. M. Dziedzic, T. Yamane, *Nature* **1987**, *330*, 769.
[10] P. Y. Chiou, A. T. Ohta, M. C. Wu, *Nature* **2005**, *436*, 370.
[11] Q. Shi, H. Xia, P. Li, Y.-S. Wang, L. Wang, S.-X. Li, G. Wang, C. Lv, L.-G. Niu, H.-B. Sun, *Adv. Opt. Mater.* **2017**, *5*, 1700442.
[12] X.-F. Lin, G.-Q. Hu, Q.-D. Chen, L.-G. Niu, Q.-S. Li, A. Ostendorf, H.-B. Sun, *Appl. Phys. Lett.* **2012**, *101*, 113901.
[13] D.-D. Han, Y.-L. Zhang, J.-N. Ma, Y.-Q. Liu, B. Han, H.-B. Sun, *Adv. Mater.* **2016**, *28*, 8328.
[14] H. Lee, A. M. Purdon, V. Chu, R. M. Westervelt, *Nano Lett.* **2004**, *4*, 995.
[15] T. P. Hunt, D. Issadore, R. M. Westervelt, *Lab Chip* **2008**, *8*, 81.
[16] M. Donolato, P. Vavassori, M. Gobbi, M. Deryabina, M. F. Hansen, V. Metlushko, B. Ilic, M. Cantoni, D. Petti, S. Brivio, R. Bertacco, *Adv. Mater.* **2010**, *22*, 2706.
[17] S. Anandakumar, V. S. Rani, S. Oh, B. L. Sinha, M. Takahashi, C. Kim, *Biosens. Bioelectron.* **2010**, *26*, 1755.
[18] K. Gunnarsson, P. E. Roy, S. Felton, J. Pihl, P. Svedlindh, S. Berner, H. Lidbaum, S. Oscarsson, *Adv. Mater.* **2005**, *17*, 1730.
[19] B. Lim, V. Reddy, X. Hu, K. Kim, M. Jadhav, R. Abedini-Nassab, Y.-W. Noh, Y. T. Lim, B. B. Yellen, C. Kim, *Nat. Commun.* **2014**, *5*, 3846.
[20] G. Katsikis, J. S. Cybulski, M. Prakash, *Nat. Phys.* **2015**, *11*, 588.
[21] H. Xia, J. Wang, Y. Tian, Q.-D. Chen, X.-B. Du, Y.-L. Zhang, Y. He, H.-B. Sun, *Adv. Mater.* **2010**, *22*, 3204.
[22] R. Mhanna, F. Qiu, L. Zhang, Y. Ding, K. Sugihara, M. Zenobi-Wong, B. J. Nelson, *Small* **2014**, *10*, 1953.
[23] X. Ding, S.-C. S. Lin, B. Kiraly, H. Yue, S. Li, I.-K. Chiang, J. Shi, S. J. Benkovic, T. J. Huang, *Proc. Natl. Acad. Sci. USA* **2012**, *109*, 11105.
[24] D. J. Collins, B. Morahan, J. Garcia-Bustos, C. Doerig, M. Plebanski, A. Neild, *Nat. Commun.* **2015**, *6*, 8686.
[25] D. Di Carlo, L. Y. Wu, L. P. Lee, *Lab Chip* **2006**, *6*, 1445.
[26] R. Burger, P. Reith, G. Kijanka, V. Akujobi, P. Abgrall, J. Ducrée, *Lab Chip* **2012**, *12*, 1289.
[27] D.-D. Han, Y.-L. Zhang, Y. Liu, Y.-Q. Liu, H.-B. Jiang, B. Han, X.-Y. Fu, H. Ding, H.-L. Xu, H.-B. Sun, *Adv. Funct. Mater.* **2015**, *25*, 4548.
[28] D.-D. Han, Y.-L. Zhang, H.-B. Jiang, H. Xia, J. Feng, Q.-D. Chen, H.-L. Xu, H.-B. Sun, *Adv. Mater.* **2015**, *27*, 332.
[29] C. Lv, H. Xia, Q. Shi, G. Wang, Y.-S. Wang, Q.-D. Chen, Y.-L. Zhang, L.-Q. Liu, H.-B. Sun, *Adv. Mater. Interfaces* **2017**, *4*, 1601002.
[30] M. S. Cohen, H. Chang, *Proc. IEEE* **1975**, *63*, 1196.
[31] R. Abedini-Nassab, D. Y. Joh, M. A. Van Heest, J. S. Yi, C. Baker, Z. Taherifard, D. M. Margolis, J. V. Garcia, A. Chilkoti, D. M. Murdoch, B. B. Yellen, *Adv. Mater.* **2015**, *27*, 6176.
[32] X. Hu, S. R. Torati, A. I. Shawl, B. Lim, K. Kim, C. Kim, *IEEE Magn. Lett.* **2016**, *7*, 1.
[33] S. Rampini, D. Kilinc, P. Li, C. Monteil, D. Gandhi, G. U. Lee, *Lab Chip* **2015**, *15*, 3370.
[34] P. Tierno, S. V. Reddy, M. G. Roper, T. H. Johansen, T. M. Fischer, *J. Phys. Chem. B* **2008**, *112*, 3833.
[35] B. B. Yellen, R. M. Erb, H. S. Son, R. Hewlin, H. Shang, G. U. Lee, *Lab Chip* **2007**, *7*, 1681.
[36] G. Vieira, T. Henighan, A. Chen, A. J. Hauser, F. Y. Yang, J. J. Chalmers, R. Sooryakumar, *Phys. Rev. Lett.* **2009**, *103*, 128101.
[37] P. Li, A. Mahmood, G. U. Lee, *Langmuir* **2011**, *27*, 6496.
[38] X. Hu, R. Abedini-Nassab, B. Lim, Y. Yang, M. Howdyshell, R. Sooryakumar, B. B. Yellen, C. Kim, *J. Appl. Phys.* **2015**, *118*, 203904.
[39] X. Hu, S. R. Goudu, S. R. Torati, B. Lim, K. Kim, C. Kim, *Lab Chip* **2016**, *16*, 3485.
[40] J. Lipfert, J. W. J. Kerssemakers, T. Jager, N. H. Dekker, *Nat. Methods* **2010**, *7*, 977.
[41] P. Lebel, A. Basu, F. C. Oberstrass, E. M. Tretter, Z. Bryant, *Nat. Methods* **2014**, *11*, 456.
[42] Y. Yang, R. M. Erb, B. J. Wiley, S. Zauscher, B. B. Yellen, *Nano Lett.* **2011**, *11*, 1681.
[43] M. U. Kopp, A. J. de Mello, A. Manz, *Science* **1998**, *280*, 1046.